FULL PAPER

# Insights into Nanoscale Electrochemical Reduction in a Memristive Oxide: the Role of Three-Phase Boundaries

*Christian Lenser,* Marten Patt, Stephan Menzel, Annemarie Köhl, Carsten Wiemann, Claus M. Schneider, Rainer Waser, and Regina Dittmann*

**The nanoscale electro-reduction in a memristive oxide is a highly relevant field for future non-volatile memory materials. Photoemission electron microscopy is used to identify the conducting filaments and correlate them to structural features of the top electrode that indicate a critical role of the three phase boundary (electrode-oxide-ambient) for the electro-chemical reduction. Based on simulated temperature profiles, the essential role of Joule heating through localized currents for electro-reduction and morphology changes is demonstrated.**

## 1. Introduction

Transition metal oxides (TMOs) have been the object of intense research in the field of electronic oxides, particularly with regard to the resistance changes during electrical treatment, known as resistive switching.[1,2] The resistive switching effect in $SrTiO_3$ (STO)—often referred to as a model-system for perovskite oxides—is generally attributed to a localized reduction, which introduces oxygen vacancies $V_O^{**}$ into the material. These act as n-dopants and contribute electrons into the conduction band. The spectral footprint of these conduction band electrons is the presence of $Ti^{3+}$ ions, indicating a $d^1$ electron configuration and therefore occupied states in the conduction band. The mechanism for this reduction is much discussed in literature, and it is generally accepted that oxygen migration under an applied electric field leads to the removal of oxygen from the oxide lattice during the first electrical stimulus (called "forming").[1,3–5]

Dr. C. Lenser, M. Patt, Dr. S. Menzel, A. Köhl, Dr. C. Wiemann, Prof. C. M. Schneider, Prof. R. Waser, Prof. R. Dittmann
Peter Grünberg Institute, Research Center Jülich
52425 Jülich, Germany
E-mail: c.lenser@fz-juelich.de
Prof. C. M. Schneider, Prof. R. Waser
Research Center Jülich, JARA-FIT
52425 Jülich, Germany
Prof. C. M. Schneider
University of Duisburg-Essen
Faculty of Physics
D-47048 Duisburg, Germany
Prof. R. Waser
Institute of Materials in Electrical Engineering and Information Technology II
RWTH Aachen University
D-52056 Aachen, Germany

DOI: 10.1002/adfm.201304233

Detecting electric field induced Ti-reduction in $SrTiO_3$ by spectroscopic means has proven a major challenge, mainly due to the fact that very low concentrations of oxygen vacancies cause significant conductivity in the material, while the overall concentration of $Ti^{3+}$ remains below the detection limit of most X-ray spectroscopies (≈1%). Hard X-ray absorption spectroscopy of transition metal dopants (such as Fe or Cr) has been shown to be a viable way to detect valence changes in STO after chemical reduction, which has been attributed to the high bond enthalpy of the Ti–O bond and correspondingly, a preferred association of oxygen vacancies to transition metal dopants.[6] In metal-insulator-metal (MIM) structures, investigations of transition metal dopants with spectroscopy techniques that enable a spatial resolution on the µm-scale,[3,7] and recent investigations into the nanoscale conductivity and the corresponding localized chemical changes,[4,8] have shed light onto the switching mechanism in Fe-doped STO (FeSTO) and hinted at the possibility that the cation sublattice may be involved in the resistance change.

In this article, we demonstrate a chemical reduction on the nanometer scale in formed FeSTO devices, induced by a combination of a large electrical potential gradient and Joule heating. Based on observations made by chemically sensitive photoemission electron microscopy in X-ray absorption mode (XPEEM), we suggest that the phase-boundary between noble-metal electrode and oxide could play a major role for the removal of oxygen ions from the device. Furthermore, we demonstrate structural changes in the cation sublattice on the surface, which is a clear indication of the importance of the local temperature during the forming process.

## 2. Results

**Figure 1** shows the electrical characteristics of the forming process induced by a quasistatic $I(V)$-sweep. The initially high resistance of the stack ($>10^{12}$ Ω) breaks down at a voltage of +7 V, forming into a low resistance state ($10^6$ Ω) in agreement with the "eightwise" polarity described by Muenstermann et al.[8] The micro-structural changes taking place during the forming can be illustrated by electron microscopy. **Figure 2** a) depicts an electron microscopy image of the electrode after electrical treatment (see Figure 1), recorded in a conventional scanning electron microscope (SEM). The Au electrode shows

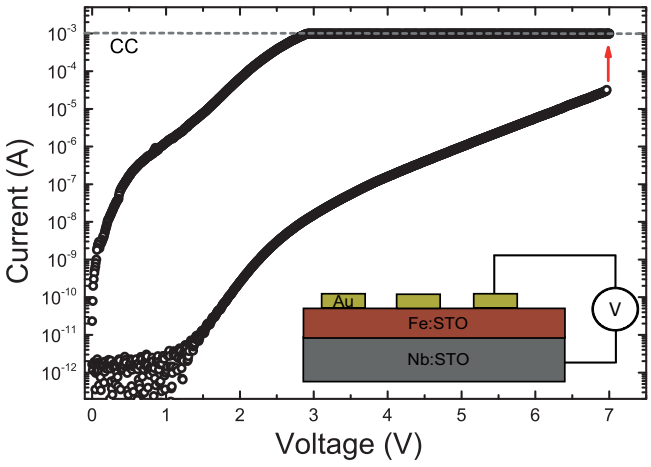


**Figure 1.** Forming sweep of the Au/FeSTO/NbSTO memristive device, with the current compliance set to 1 mA. The inset shows a scheme of the sample geometry. The bottom electrode (NbSTO) was grounded, and bias applied to the top electrode (Au).

two distinctive features, marked "A" and "B". Feature "A" is a scratch in the electrode caused by the W-probe used to establish electrical contact, whereas feature "B" appeared after the current jump marked by the red arrow in Figure 1, and is therefore related to the resistance change. Feature "B" (hereafter called the forming crater) shows a remarkable contrast pattern, depicted in higher magnification in Figure 2b), which is most likely caused by local variations of the work function (electron affinity), for example, through the doping level.[9]

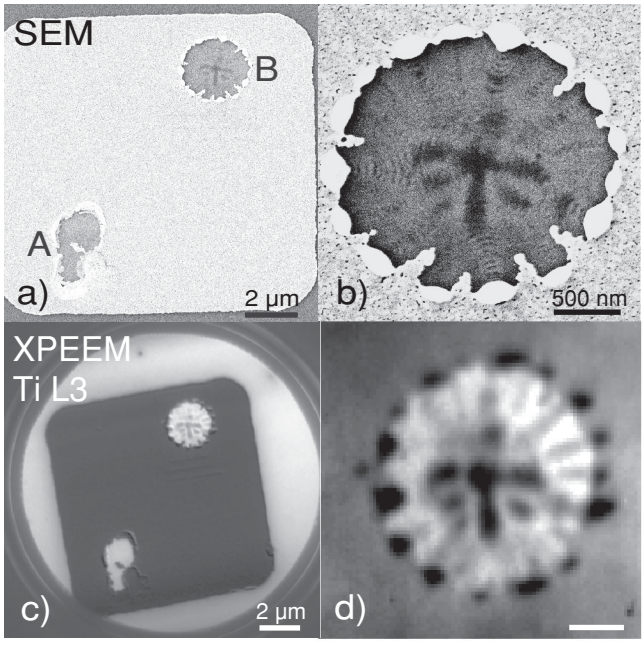


**Figure 2.** a) SEM image of the formed electrode. Features "A" and "B" mark the contact point of the probe and forming crater, respectively, with an higher magnification image of the crater in (b). c) Electron microscopy image recorded by XPEEM of the same electrode, with an excitation energy of $h\nu = 459.5$ eV, corresponding to the $e_g$ level of the Ti $L_3$ edge. Inhomogeneities are visible in the forming crater (feature "B"), where feature "A" is completely homogeneous. A zoom on the crater is shown in (d).

A similar image was recorded by XPEEM, at an excitation energy of $h\nu = 459.5$ eV, as shown in Figure 2c). This excitation energy corresponds to the energy of the $e_g$ level of the Ti $L_3$ edge, which enhances the secondary electron yield of Ti ($\delta_{Ti}$) through resonant absorption. As a consequence, $\delta_{Ti}$ is higher at this energy than $\delta_{Au}$, reversing the contrast that is normally observed between Au and Ti.[10] Furthermore, the PEEM image shows a contrast pattern in the forming crater that is almost identical to that observed by SEM, indicating possible chemical inhomogeneities.

A closer examination of the forming crater by SEM and PEEM reveals additional details, as shown in Figure 2b,d, respectively. The forming crater has a diameter of approximately 2 µm and is circular in shape. The rim of the crater is decorated with globules of Au, which can be seen as bright areas in the SEM image and dark areas in the PEEM image.[11] The smooth, rounded character of these globules strongly indicates that Au from the crater location has been enabled to flow in a liquid-like state to the crater rim. It is important to note that despite the structural damage to the electrode during forming, the low resistance state persists and is reversible by the application of a negative voltage to the top electrode.

To correlate the structural changes with the local chemical state of the oxide, we have performed X-ray absorption spectroscopy (XAS) of the Ti $L_{2,3}$-edge, Fe $L_{2,3}$-edge and Sr $M_{4,5}$-edge at high resolution in the PEEM. To extract spectral information from the PEEM image stacks recorded during the XAS scan, several regions of interest (ROI) are defined in the image, and the spectral intensity is extracted from the brightness of each pixel in the ROI. The Ti L-edge absorption spectra recorded in the forming crater are presented in **Figure 3**a), with the corresponding regions of interest (ROI) marked in the PEEM image in the inset. The reference spectrum (black line) was recorded on the FeSTO film that was uncovered by the W-probe contact (feature "A" in Figure 2). Due to the ion beam etching involved in the fabrication of the electrodes, the surrounding material is not a suitable reference for the measurements.

The reference spectrum shows the spin-orbit split components of the Ti $L_{2,3}$ absorption edge, which are in turn split into two components due to the crystal field of the octahedral oxygen coordination of the B-site ions in STO. The spectrum is in very good agreement with spectra reported for tetravalent Ti ions in STO.[12] In contrast, ROI-2 (red line, marked red in the inset) clearly shows a shoulder at the $L_3$ $e_g$ line, as well as a much more shallow dip between the two components of the $L_2$ edge, indicating at least one additional spectral component in both edges. The energy separation of the new component and the $L_3$ $t_{2g}$ level is much smaller (1.5 eV) than that of the STO crystal field, which is 2.3 eV. The significant spectral contribution between the $t_{2g}$ and $e_g$ lines, as well as added intensity in the pre-edge region below the $L_3$ $t_{2g}$ line, are similar to the observations made by Abbate *et* al. on La-substitution of Sr in the STO matrix, marking a clear indication of a valence change at the Ti-site from $Ti^{4+}$ to $Ti^{3+}$.[13]

The Ti L-edge spectrum arising from ROI-1 (blue line, marked in the inset) is very similar to the reference spectrum, although close examination shows a slightly increased

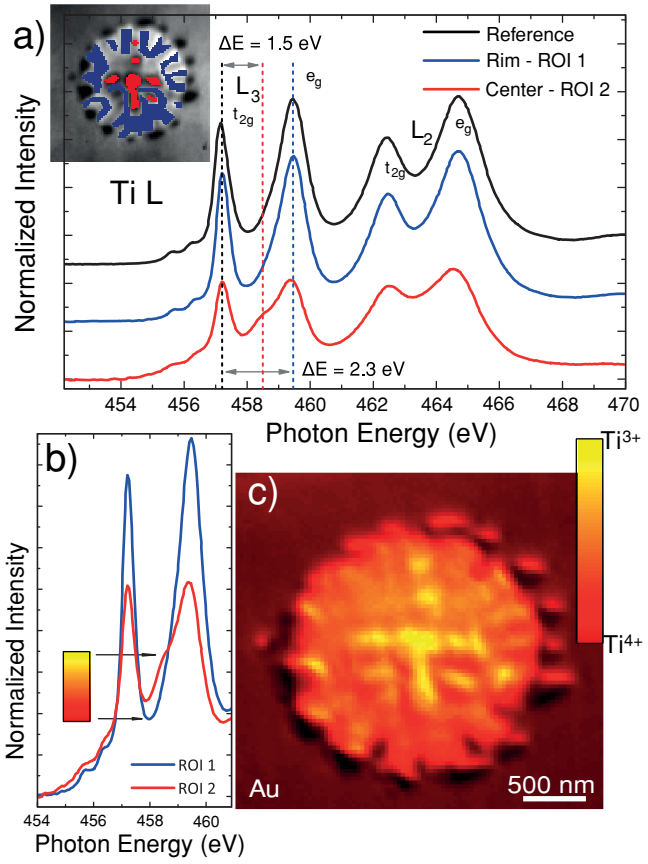


**Figure 3.** a) Ti L-edge absorption spectra recorded in the three regions of interest: ROI 1 ("rim", blue) and ROI 2 ("center", red), as well as a reference spectrum (black) recorded in the needle contact area. Inset: PEEM image with ROI 1 and 2 marked in blue and red, respectively. b) Direct comparison of the Ti $L_3$ edge spectra from ROI 1 and 2, normalized to the background. c): False color map depicting the distribution of $Ti^{3+}$ (yellow) and $Ti^{4+}$ (red) states in the forming crater.

spectral intensity between the $t_{2g}$ and $e_g$ lines of both $L_2$ and $L_3$ edge. Regarding the strong spectral changes found in ROI-2, the most likely explanation is a very small amount of $Ti^{3+}$ in ROI-1 as well. A direct comparison of the spectra recorded in ROI-1 and ROI-2, normalized to the respective pre-edge intensity, shows the spectral differences of the Ti $L_3$ edge directly (Figure 3b). The increased intensity of the $Ti^{3+}$ shoulder between $t_{2g}$ and $e_g$ components facilitates a spatial distinction of lightly (ROI-1) and heavily (ROI-2) reduced regions in the PEEM image, displayed as a false color image in Figure 3c).[14] The yellow regions correspond to a strong contribution of the $Ti^{3+}$ component, while the red regions indicate the absence of this component, as marked by the color bar in Figure 3b). With this iterative analysis, it is possible to first isolate chemically different regions by selected ROIs, and consecutively use the spectral differences to spatially resolve the Ti oxidation state in the complete forming crater. The heavily reduced regions marked in yellow clearly coincide with the dark regions (low secondary electron yield) observed in the SEM and resonant XPEEM images (Figure 2), reinforcing the assumption that the contrast is caused by a variation of the local doping level and (corresponding) changes in the work function (or electron

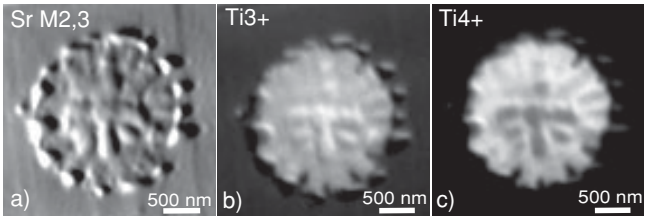


**Figure 4.** a) PEEM image recorded at the Sr $M_{4,5}$ edge, normalized to the background intensity and averaged from 268.4–269.15 eV. b) PEEM image recorded between the $t_{2g}$ and $e_g$ components of the Ti $L_3$ edge (averaged from 457.7–458.6 eV), with light regions corresponding to the presence of $Ti^{3+}$. c) PEEM image averaged from 457.0–457.4 eV, corresponding to the $t_{2g}$ component of the Ti $L_3$ edge. Bright regions mark $Ti^{4+}$.

affinity). Figure 3b) indicates that the overall intensity of the $Ti^{3+}$ component is smaller than that of the $Ti^{4+}$ component. Since the image normalization removes the work-function contrast, the intensity difference can be attributed to a lower amount of Ti ions in the probed volume. Interestingly, images recorded at the Sr $M_{4,5}$-edge show the same intensity contrast after normalization as the $Ti^{3+}$ sensitive PEEM image, which is inverted in comparison to the $Ti^{4+}$ sensitive image (**Figure 4**a–c, respectively). From these images, it follows qualitatively that the amount of Sr is larger in the center of the crater (ROI-2) than in the rim regions (ROI-1). The overall Ti concentration is lowered, but at the same time the fraction of $Ti^{3+}$ ions is enhanced in the Sr-enriched regions. We attribute this to the presence of a Sr-rich surface layer that is formed during the reduction process, which attenuates the Ti signal but enhances the Sr signal. Similar observations have been made for switched FeSTO surfaces recently.[4] Furthermore, surface segregation of Sr in perovskite oxides is found at elevated temperatures for several material systems, such $SrTiO_3$ and $La_{1-x}Sr_xCoO_3$,[15,16] and seems to be a general phenomenon for doped perovskite oxides.[17]

**Figure 5** demonstrates that the chemical changes observable at the Fe-dopants are much more pronounced than at the Ti host cations. Similar to the Ti L-edge, the Fe L-edge was extracted from the images in three different ROIs: a reference

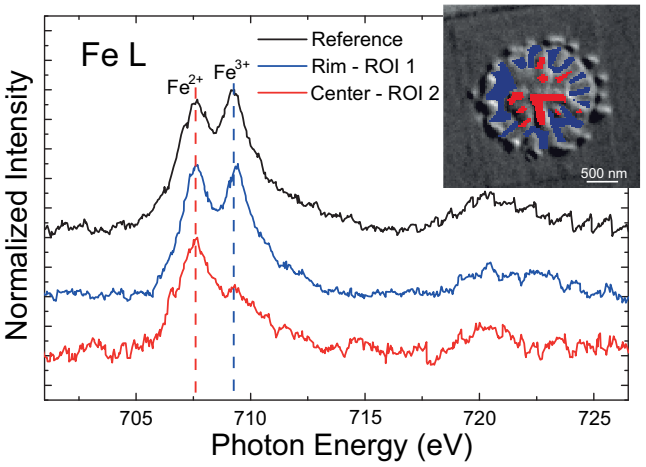


**Figure 5.** Fe L-edge spectra recorded in the two ROI, as indicated in the inset, and the reference position. The ROI correspond roughly to the ROI defined for Ti.

spectrum, the lightly reduced rim of the crater (ROI-1) and the heavily reduced center (ROI-2), indicated by blue and red markings, respectively, in the Fe L-edge PEEM image shown in the inset of Figure 5. The spectrum recorded at the reference location consists of two spectral components at the $L_3$-edge, corresponding to a mixed valence state of $Fe^{2+}/Fe^{3+}$, while no $Fe^{4+}$-related signal is detected, in agreement with previous investigations of such thin films.[3,18] In the reduced center of the crater (ROI-2), the absence of the higher energy peak in the $L_3$ edge demonstrates the prevalence of the divalent oxidation state $Fe^{2+}$, while the spectrum recorded in ROI-1 indicates a slight reduction of the crater rim due to the slight intensity decrease of the $Fe^{3+}$ line, relative to the $Fe^{2+}$ line. The analysis of the Fe L-edge therefore supports the findings observed at the Ti L-edge, as expected.

On the basis of the electron microscopy investigations, we point out three major observations: i) the Au electrode has been structurally altered, with indications of a liquid-like state, ii) nanoscale reduction is observable on the B-site cations in the dark regions of the SEM images and iii) indications for an enrichment of Sr on the surface of the reduced regions can be deduced from the XPEEM intensity. We suggest that all three of these phenomena are related to a local temperature increase through Joule heating, as it has been discussed for similar MIM-structures and other material systems.[19–21] It follows that the dark wedges are the exits of conductive filaments on the sample surface. With these observations in mind, it is possible to discuss the pattern in which the reduction reaction takes place in the crater.

In order to examine the evolution of the nanoscale structure more clearly, **Figure 6**a) shows a high resolution SEM image of another electrode after the same forming procedure. The contact point of the needle is marked with "A", and the nearby forming crater is located at the edge of the electrode. The center of the crater is marked with an orange circle (feature "B"), with traces, consisting of individual, curved wedges (marked with a green circle), extending out from their origin at the center toward the Au globules (blue circle) visible at the edge of the crater, exemplary marked with "C". The nanoscale intensity contrast visible in the SEM image is in principle identical to that of the forming crater analyzed with XPEEM, and can be observed in every forming crater examined for this study. The feature we will focus on are the clearly distinguishable, half-moon shaped wedges showing a dark intensity contrast in the SEM image.

To clarify whether the Joule heating can account for a sufficient temperature increase to enable cation movement and melt the Au electrode, we have performed electro-thermal simulations based on the transient heat equation and the continuity equation (for details of the simulation, see reference[20] and the supplementary information) using voltage and current values extracted from the I(V)-characteristics given in Figure 1.

First, we studied the Joule heating effect during the current jump at 7 V. For this we assumed a single, cylindrical conducting filament within the Fe-doped STO layer. The filament diameter was chosen to be 45 nm according to the size of the center of the crater. The maximum current flowing through the device is varied from 30 µA to 1 mA while the filament conductivity is adapted in order to achieve a constant voltage drop of 7 V. Since the electrical conductivity of the filament is higher than the surrounding insulating matrix, all power is dissipated within the filament and Joule heating comes into effect. Figure 6b) shows the temperature increase at the interface between the conducting filament and the Au electrode for increasing maximum current. The interface becomes sufficiently hot to melt the Au electrode electrode for $I_{max} > 150$ µA. The local temperature decreases radially from the center of the filament/Au electrode interface (cf. Figure 6b) which enables a radial, outward motion of Au in a way reminiscent of the

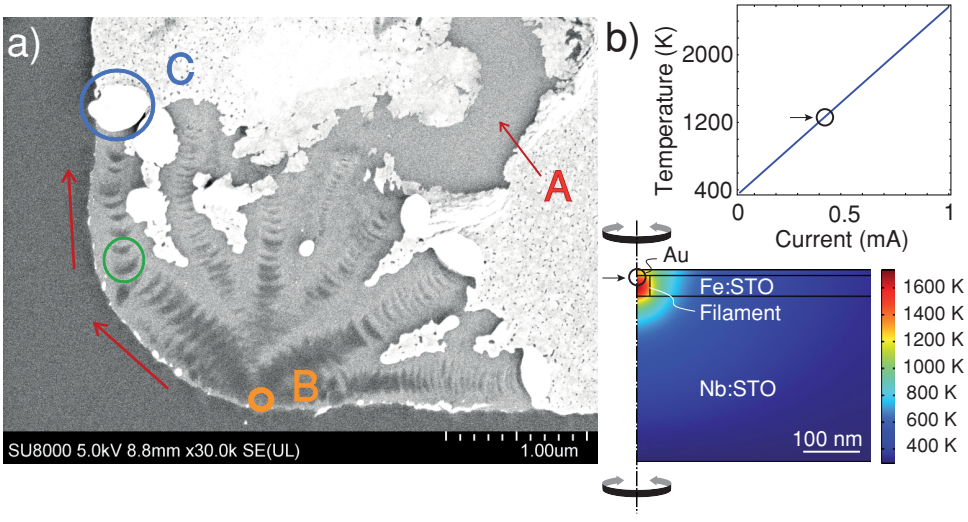


**Figure 6.** a) SEM image of a forming crater on a separate electrode. Marked features correspond to the needle contact point (A), the center of the forming crater (which is equivalent to the position of the initial filament, B) and the Au globules present after the forming has stopped (C). The green circle marks two exemplary filaments. b) Calculated temperature as a function of current (T(I)) at the Au/FeSTO interface as a function of current through a single filament, and a side view of the temperature distribution around the filament. The temperature is extracted for the location marked with circle and arrow in the side-view, while the temperature scale for the side-view is extracted for the working point marked in the T(I) plot.

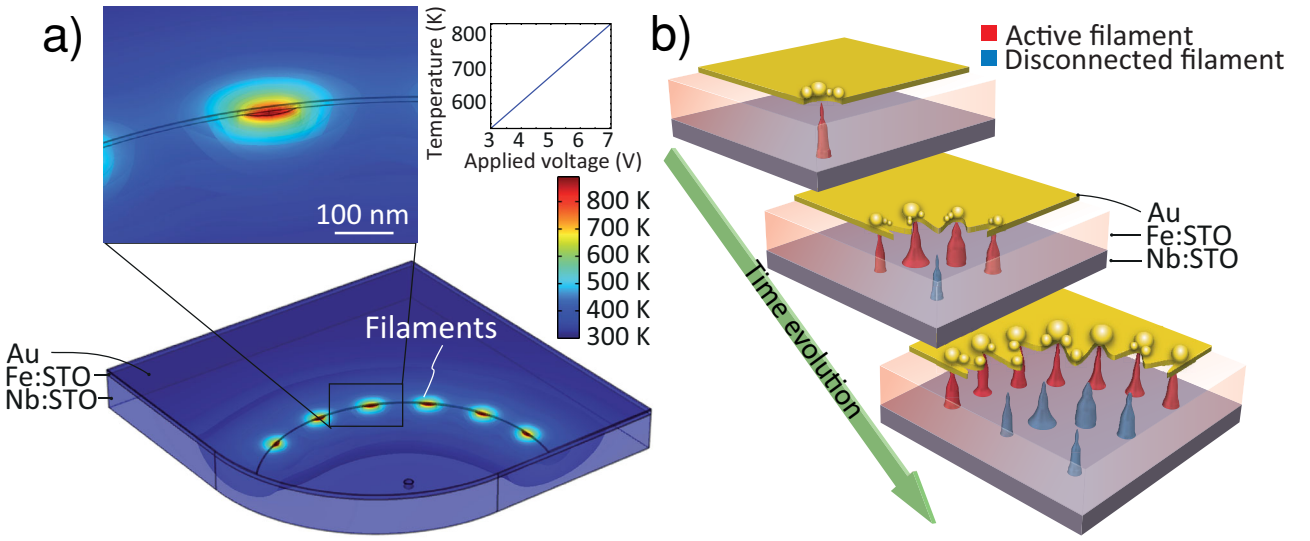


**Figure 7.** a) 3D calculation of the local temperature for the theoretical case of six filaments conducting a current of 1 mA in parallel. The inset shows the local temperature at each Au/FeSTO interface as a function of applied voltage for a constant current. The zoom-in shows the temperature distribution around a single filament, which is half covered by the Au electrode. b) Schematic representation of the time evolution of the forming crater, indicating the growth of the crater and the concomitant formation of additional filaments at each position of the electrode edge.

Bérnard-Marangoni convection (mass transfer under a temperature and concomitant surface tension gradient).[22]

In a second simulation study, we examine the Joule heating effect while the current is limited by the compliance. Here, we assume a three dimensional geometry that represents a later stage of the forming process. The Au electrode does not cover the whole Fe-doped STO anymore and 6 active wedge-shaped filaments are assumed at the Au electrode rim. The original cylindrical filament is now disconnected. For the simulations the voltage is changed from +7 V to +2.75 V while the filament conductivity is adapted to achieve a constant maximum device current of 1 mA. The simulated temperature distribution shown in **Figure 7**a) reveals that significant Joule heating occurs in this scenario as well. Again, the hottest spots are at the center of the filaments and the temperature decreases radially outward. The local temperature at the filament/Au interface decreases with decreasing voltage as less power is dissipated, until the forming process stops. Note that the simulated scenario can be regarded as a worst-case scenario since all filaments are contributing equally to the overall current. If the filaments contribute unequally or if fewer filaments are connected at the same time, the local temperature will be even higher in those filaments carrying the major current.

These considerations show that for the given voltage and current values, a sufficiently high local temperature increase can be expected to enable the movement of Sr, as well as the melting of the Au electrode. We therefore assume Joule heating to be the cause of the observed effects.

## 3. Discussion

From the contrast pattern visible in the crater, we can reconstruct the spatial and temporal evolution of the nanoscale reduction process. A schematic visualization is displayed in Figure 7b, based on the geometry of the SEM image given in Figure 6a). We start by assuming that the reduction reaction takes place initially at the center of the crater. Prior to the forming (before a complete filament is formed), the current flows through the entire electrode area. The laterally inhomogeneous conductivity of FeSTO thin films causes the current flow to be enhanced in confined "pre-filaments",[23–25] which can be either related to local differences in the doping level or structural defects, like screw dislocations.[26] Above a certain critical current density in the pre-filaments, the electro-reduction takes place through a self-accelerated process where Joule heating leads to enhanced mobility of the oxygen ions, which accelerates the reduction, which in turn enhances the conductivity of the filaments and therefore the Joule heating. Pre-existing defects play an important role in determining where the filament is formed,[26] as well as the ability of the MIM stack to dissipate the generated heat.[27]

As soon as a significant current starts to flow and a filament is formed, the localized Joule heating melts the Au electrode, causing it to flow away from the "hot spot" through a gradient of the surface tension induced by the localized temperature increase (similar to Bérnard-Marangoni convection).[22] The mobile Au forms small globules and retreats away from the hot spot of the first filament, along the traces visible in the SEM image (exemplary marked by the two red arrows in Figure 6a). As soon as the Au has retreated from a reduced region due to local heating, the electrical contact to the conducting filament is disconnected, and new filaments are formed at the new edge of the electrode. The fact that these disconnected filaments are arranged along the traces reveals that the Au globules do not reach their final position immediately, but that filaments are formed sequentially. The important point here is that filaments are formed only at the edge of the Au electrode at any given time, as indicated in Figure 7b. We note that for different experimental geometries, in particular a higher film thickness,

the nucleation and growth of new filaments from the disconnected filament (acting as an extended electrode) might be preferred over the growth of new filaments between bottom and top electrode. For our case, the low film thickness insures that the largest gradient of the electrical potential occurs across the film, and that new filaments are grown between bottom and top electrode.

This process terminates as soon as the current flowing through the filaments is too low to supply a sufficiently large quantity of heat. We suggest that this point is reached as soon as the current compliance of our semiconductor analyzer comes into effect, which we estimate to a few µs. In the final position, the active filaments are covered, at least partially, by the Au electrode. The lateral size of the filaments is on the order of 100 nm or less. Interestingly, a small finger of Au protrudes into the circle between each the trace of filaments left by each globule (cf. Figure 6a). This indicates that the temperature needed for the melting of the Au electrode is indeed caused by the localized current, and the top electrode is heated only close to the conducting filaments.

We note that while our experiments demonstrate clearly the presence of multiple conductive filaments, a macro-scale analysis with insufficient spatial resolution would only find evidence of localized conduction, which is regularly regarded as proof of a single filament.

The role of Joule heating in FeSTO has been discussed by Menzel et al. and shown to be essential for high switching speeds by providing additional mobility to the anions in the lattice.[21] However, the thermal stress that the localized current induces in the metal electrode may very well play a critical role in the switching process as well. As we show in the presented investigation, the localized reduction of the material takes places only at an electrode edge, which is usually the physical edge of the electrode or a defect in the electrode that is widened by the mechanism described above. These edges represent a triple phase boundary (TPB), where oxide, metal and the ambient atmosphere are in contact. The TPB facilitates the release of oxygen gas, marking these areas as preferred reduction sites. Such electrode damage during forming has been observed in previous investigations,[28–31] and is not restricted to epitaxial oxide systems, but can also be encountered in technologically relevant systems such as nanocrystalline or amorphous oxides.

## 4. Conclusion

By a combined approach using scanning electron microscopy (SEM) and X-ray photoemission electron microscopy (XPEEM), we have examined the structural changes in a formed Au/FeSTO/ NbSTO device and elucidated the combined effect of an applied electric field and local Joule heating. We have assessed the magnitude of the expected temperature increase, and found it to be sufficiently high to induce both the observed ionic mobility on the cation sublattice of the oxide and mass transport in the Au electrode. The lowered electrical resistance is a consequence of nanoscale chemical reductions in the FeSTO, accompanied by a segregation of Sr to the surface. We demonstrate that the reduction reaction takes places at the three phase boundary (TPB) formed by the electrode, oxide and ambient atmosphere exclusively, which points to important ramifications for the role that the nanoscale structure of the top electrode can play for the resistive switching in oxidic MIM structures.

## 5. Experimental Section

Epitaxial $SrTi_{0.95}Fe_{0.05}O_3$ films of 20 nm thickness were grown on conducting Nb:STO substrates via pulsed laser deposition (PLD) at a substrate temperature of 700°C, oxygen pressure $p_{o2} = 0.25$ mbar and a laser fluency of 0.8 J cm$^{-2}$. Subsequently, the oxide film was covered in–situ with a 6 nm Au layer, deposited by magnetron sputtering at room temperature under flowing Ar gas at $p = 7 \times 10^{-2}$ mbar. The Au layer was structured into 10 µm × 10 µm electrodes using optical lithography and ion beam etching. Electrical characterization of the MIM structures was performed with an Agilent B 1500A semiconductor analyzer, utilizing tungsten whisker-probes to establish contact.

Scanning electron microscopy (SEM) of the switched samples was done using a Hitachi SU 8000 field-emission electron microscope. The X-ray photoemission electron microscopy (XPEEM) was performed at the Nanospectroscopy beamline at the ELETTRA synchrotron laboratory (Trieste, Italy), using the spectroscopic photoemission and low-energy electron microscope (SPELEEM).[32] All images were acquired in the X-ray absorption spectroscopy (XAS) mode using secondary electrons as the detection signal. The photon energy $E_{ph}$ was increased in steps of 50 meV over the Ti L-edge ($E_{ph}$ = 452–470 eV) and the Fe L-edge ($E_{ph}$ = 700–730 eV), and a microscopic image of the secondary electron yield was taken at each photon energy. The spatial resolution of the microscope was set to approx. 50 nm whereas the spectral resolution of the beamline was approx. 0.61 eV for the Ti L-edge and 1.10 eV for the Fe L-edge measurement. Image analysis and spectral extraction was performed using the SpeLeem Image Suite (SIS) in the environment of the IGOR Pro software package.

## Supporting Information

Supporting Information is available from the Wiley Online Library or from the author.

## Acknowledgements

The authors would like to thank A. Locatelli and the beamline staff at the Nanospectroscopy beamline for support and access to the instrument, as well as M. Apel for helpful discussions. Financial support through SFB 917 "Nanoswitches" is gratefully acknowledged.

Received: December 19, 2013
Revised: February 17, 2014
Published online: April 19, 2014

[1] R. Waser, M. Aono, *Nat. Mater.* **2007**, *6*, 833.
[2] R. Waser, R. Dittmann, G. Staikov, K. Szot, *Adv. Mater.* **2009**, *21*, 2632.
[3] Ch. Lenser, A. Kuzmin, J. Purans, A. Kalinko, R. Waser, R. Dittmann. *J. Appl. Phys.* **2012**, *111*, 076101.
[4] R. Dittmann, R. Muenstermann, I. Krug, D. Park, T. Menke, J. Mayer, A. Besmehn, F. Kronast, C. M. Schneider, R. Waser. *Proc. IEEE* **2012**, *100*, 1979.
[5] K. Szot, W. Speier, G. Bihlmayer, R. Waser, *Nat. Mater.* **2006**, *5*, 312.
[6] B. P. Andreasson, M. Janousch, U. Staub, T. Todorova, B. Delley, G. I. Meijer, E. Pomjakushina, *Phys. Rev. B* **2009**, *80*, 212103.

[7] M. Janousch, G. I. Meijer, U. Staub, B. Delley, S. F. Karg, B. P. Andreasson, *Adv. Mater.* **2007**, *19*, 2232.
[8] R. Muenstermann, T. Menke, R. Dittmann, R. Waser, *Adv. Mater.* **2010**, *22*, 4819.
[9] J. Cazaux, *Ultramicroscopy* **2010**, *110*, 242.
[10] Under non-resonant conditions, $\delta_{Au} > \delta_{Ti}$.
[11] The brighter intensity in the SEM image is due to the increased amount of Au in the scattering cone of the primary electrons, and the fact that for a heavy element such Au, the secondary electron (SE) yield from backscattered electrons (BSE) is higher than that from primary electrons. In the resonant PEEM image, there are no BSE due to the excitation with photons. The Au globules appear darker than the Au film for every excitation energy, which is a consequence of the distortion of the electric field lines between globules and the immersion lens of the microscope.[33]
[12] F. M. F de Groot, J. C. Fuggle, B. T. Thole, G. A. Sawatzky, *Phys. Rev. B* **1990**, *41*, 928.
[13] M. Abbate, F. M. F. deGroot, J. C. Fuggle, A. Fujimori, Y. Tokura, Y Fujishima, O. Strebel, M. Domke, G. Kaindl, J. van Elp, T. Thole, G. A. Sawatzky, M. Sacchi, N. Tsuda, *Phys. Rev. B* **1991**, *44*, 5419.
[14] This map of the local oxidation state of Ti was generated by averaging several images over the energy range between the peaks (457.7–458.6 eV), and displaying the image intensity using a color scheme. Note that the dark red region around the forming crater is covered by Au, and therefore no Ti is visible.
[15] Z. Cai, M. Kubicek, J. Fleig, B. Yildiz, *Chem. Mater.* **2012**, *24*, 1116.
[16] K. Szot, W. Speier, U. Breuer, R. Meyer, J. Szade, R. Waser, *Surf. Sci.* **2000**, *460*, 112.
[17] W. Lee, J. W. Han, Y. Chen, Z. Cai, B. Yildiz, *J. Am. Chem. Soc.* **2013**, *135*, 7909.
[18] A. Koehl, D. Kajewski, J. Kubacki, K. Szot, A. Kuzmin, Ch. Lenser, P. Meuffels, R. Dittmann, R. Waser, J. Szade, *Phys. Chem. Chem. Phys.* **2013**, *15*, 8311.
[19] S. H. Chang, J. S. Lee, S. C. Chae, S. B. Lee, C. Liu, B. Kahng, D. Kim, T. W. Noh, *Phys. Rev. Lett.* **2009**, *102*, 26801/1.
[20] S. Menzel, M. Waters, A. Marchewka, U. Böttger, R. Dittmann, R. Waser, *Adv. Funct. Mater.* **2011**, *21*, 4487.
[21] U. Russo, D. Ielmini, C. Cagli, A. L. Lacaita, *IEEE Trans. Electron Devices* **2009**, *56*, 186.
[22] E. Bodenschatz, W. Pesch, G. Ahlers, *Annu. Rev. Fluid Mech.* **2000**, *32*, 709.
[23] A. Koehl, H. Wasmund, A. Herpers, P. Guttmann, S. Werner, K. Henzler, H. Du, J. Mayer, R. Waser, R. Dittmann, *APL Mater.* **2013**, *1*, 042102.
[24] S. Stille, Ch. Lenser, R. Dittmann, A. Koehl, I. Krug, R. Muenstermann, J. Perlich, C. M. Schneider, U. Klemradt, R. Waser, *Appl. Phys. Lett.* **2012**, *100*, 223503.
[25] K. Szot, R. Dittmann, W. Speier, R. Waser, *Phys. Status Solidi (RRL)* **2007**, *1*, 86.
[26] Ch. Lenser, Z. Connell, A. Kovacs, R. Dunin-Borkowski, A. Koehl, R. Waser, R. Dittmann, *Appl. Phys. Lett.* **2013**, *102*, 183504.
[27] J. P. Strachan, D. B. Strukov, J. Borghetti, J. J. Yang, G. Medeiros-Ribeiro, R. S. Williams. *Nanotechnology* **2011**, *22*, 254015.
[28] D.-H. Kwon, K. M. Kim, J. H. Jang, J. M. Jeon, M. H. Lee, G. H. Kim, X.-S. Li, G.-S. Park, B. Lee, S. Han, M. Kim, C. S. Hwang, *Nat. Nanotechnol.* **2010**, *5*, 148.
[29] H. Schroeder, D. S. Jeong, *Microelectron. Eng.* **2007**, *84*, 1982.
[30] J. P. Strachan, J. J. Yang, L. A. Montoro, C. A. Ospina, A. J. Ramirez, A. L. D. Kilcoyne, G. Medeiros-Ribeiro, R. S. Williams, *Beilstein J. Nanotechnol.* **2013**, *4*, 467.
[31] J. P. Strachan, J. J. Yang, R. Muenstermann, A. Scholl, G. Medeiros-Ribeiro, D. R. Stewart, R. S. Williams, *Nanotechnology* **2009**, *98*, 485701.
[32] A. Locatelli, L. Aballe, T. O. Mentes, M. Kiskinova, E. Bauer, *Surf. Interface Anal.* **2006**, *38*, 1554.
[33] J. Stöhr, S. Anders, *IBM J. Res. Develop.* **2000**, *44*, 535.